ELSEVIER

Journal of Nuclear Materials 278 (2000) 136–148

journal of nuclear materials

www.elsevier.nl/locate/jnucmat

Examination of melted fuel rods and released core material from the first Phebus-FP reactor accident experiment

P.D.W. Bottomley, A.D. Stalios, J.-P. Glatz, B. Sätmark, C.T. Walker *

European Commission, Joint Research Centre, Institute for Transuranium Elements, P.O. Box 2340, D-76125 Karlsruhe, Germany

Received 30 June 1999; accepted 25 October 1999

Abstract

In the first Phebus test, 20, one meter long, lightly irradiated UO_2 fuel rods and a central Ag–In–Cd control rod were heated by fission power to an estimated 3000°C. In this paper results are reported for the composition of the molten corium pool in the lower part of the test assembly and deposits of released core material in the vertical line. The examination techniques used comprised optical microscopy, scanning electron microscopy, X-ray microbeam analysis, inductively coupled plasma mass spectroscopy, X-ray diffraction and γ-spectroscopy. The matrix of the corium pool was a single phase of composition $(U_{0.50}Zr_{0.47}Fe_{0.02}Y_{0.01})O_{2\pm x}$. Inclusions in the solidified pool were ReIr alloys, W with minor concentrations of Fe and Ni and spinels of Cr, Fe and Ni. The main constituents of the deposit in the vertical line were Re, Ag, In and Sn. Tin formed a thin layer on the steel surface. Droplets of the corium matrix phase were embedded in the deposit. Traces of ^{137}Cs were mainly responsible for the γ-activity of the deposit.

1. Introduction

The Phebus–FP (fission product) project is managed jointly by the Institut de Protection et Sureté Nucléaire (IPSN), Cadarache, France and the Institute for Systems, Infomatics and Safety Technologies at the European Commission's Joint Research Centre, Ispra, Italy with contributions from Canada, Japan, South Korea, the USA and, since 1995, Switzerland. The project is designed to measure the source-term (mass or activity of fission products, activation products and actinides released from a nuclear fuel in a reactor accident) and to study the degradation of irradiated UO_2 fuel in conditions typical of a severe loss of coolant accident in a pressurised water reactor (PWR). In the first test (FPT 0), performed in December 1993, a bundle of 20, 1 m long UO_2 fuel rods, which had been irradiated for 15 days, and a central Ag–In–Cd control rod were heated by fission power in the Phebus reactor at Cadarache to an estimated temperature of 3000°C over a period of 6 h.

At the Institute for Transuranium Elements a section from the bottom of the solidified corium [1] pool in the lower part of the test-assembly and deposits of released core material in the vertical line leading to the pressuriser, relief tank and steam generator simulating the PWR primary cooling system have been examined. The examination techniques used were optical microscopy, scanning electron microscopy (SEM), wavelength and energy dispersive electron probe microanalysis (EPMA), inductively coupled plasma-mass spectrometry (ICP-MS), X-ray diffraction and γ-spectroscopy. The investigation of the corium pool had the following three aims. Determination of the chemical composition of the urania–zirconia matrix phase. Identification of the metallic and oxide inclusions. Characterisation of the chemical interaction between molten corium and (1) the fuel rods, (2) the Zircaloy stiffeners and the inner zirconia thermal shroud, (3) the ThO_2 ultrasonic thermometers and the W/WRe thermocouples at the centre of some fuel rods.

* Corresponding author. Tel.: +49-7247 951 477; fax: +49-7247 951 590.

[1] Corium is a multi-phase eutectic system formed by the melting and interaction of UO_2 fuel, Zircaloy cladding, structural materials and fission products.

0022-3115/00/$ - see front matter
PII: S0022-3115(99)00257-3

The investigation of the material deposited in the vertical line had two aims. First, determination of the chemical composition of the deposits. Second, to establish, as for as possible, the chronological sequence of release and deposition during the experiment.

2. The Phebus test facility

Phebus is a loop-type reactor with a 40 MWe low enriched 'driver core' which is cooled and moderated by demineralised light water and reflected using light water and graphite. The reactor was originally built to carry out transient tests on light water reactor fuels. For the 'FP' experiments the reactor was equipped with a new cooling system and a new building was constructed adjacent to the existing reactor hall to house the simulated PWR primary circuit and containment. A schematic diagram of the test facility is shown in Fig. 1. The volume of the pressuriser, relief tank, and steam generator of the simulated primary cooling system and the volume of the containment vessel is 1/5000th of that found in a commercial nuclear power station. This volume reduction represents the ratio of the fission product inventory in the fuel rod test assembly and the fission product inventory in a 900 MWe PWR. The containment vessel that simulates the reactor containment building is a 10 m^3 tank which contains three temperature controlled cylinders (condensators) that can be used to replicate the thermal capacity of structures in the buildings of a nuclear power station.

The fuel rod test assembly is inserted in a cell at the centre of the driver core of the Phebus reactor. A steam-rich or hydrogen-rich environment during meltdown is produced by injecting water vapour and hydrogen or helium at the prescribed ratio into the assembly through feed lines at the base of the cell. The vertical line is situated above the fuel bundle and is joined to the horizontal line, which connects the reactor to the simulated primary cooling system, by way of an elbow union (see Fig. 2). The vertical line is made of a Ni-based alloy (Inconel 600) and, during the test, is held at a temperature slightly above 700°C.

A detailed description of Phebus test installation can be found in Refs. [1,2].

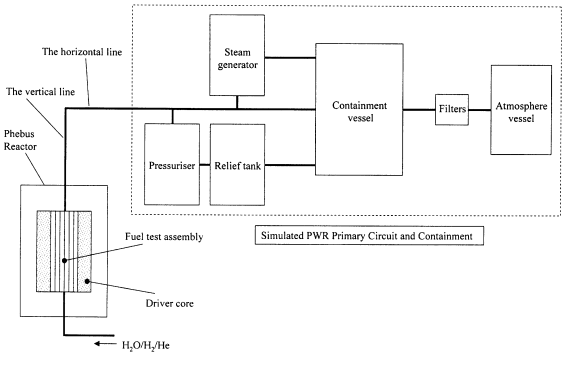

Fig. 1. Schematic diagram of the Phebus-FP test facility.

3. The FPT 0 test

The FPT 0 test assembly was a bundle of 20 unirradiated UO_2 fuel rods containing a central Ag–15In–5Cd

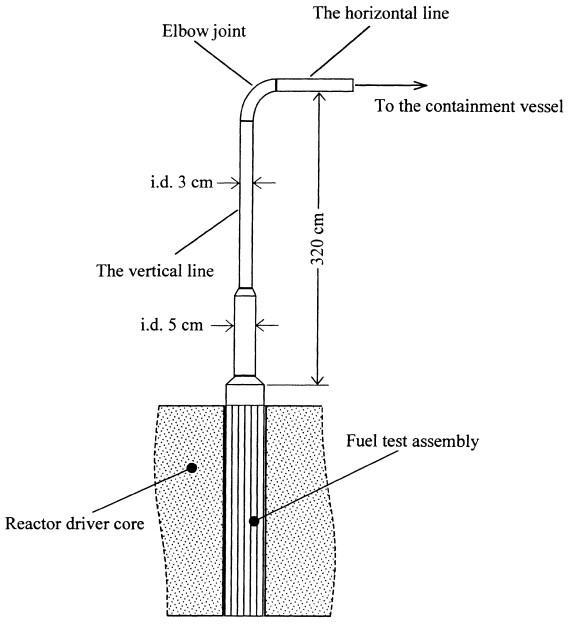

Fig. 2. The FPT 0 fuel rod test assembly and the vertical line (not to scale).

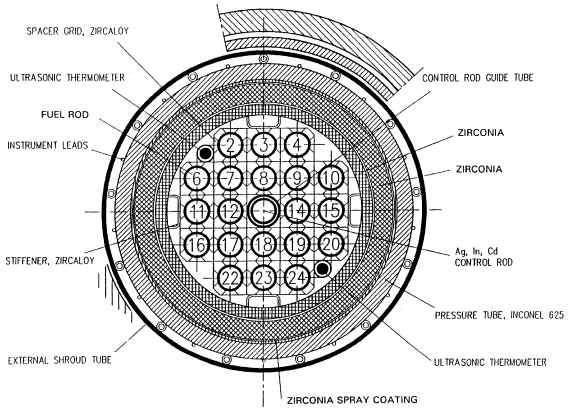

Fig. 3. Section through the FPT 0 fuel rod test assembly (after Bottomley et al. [8]).

control rod, clad with AISI 304 austenitic stainless steel (see Fig. 3). The 15 day pre-irradiation was intended to generate a small fission product inventory, including short-lived fission products for monitoring purposes, i.e., ^{131}I. The power of the driver core was steadily raised, with intermediate checks, while the coolant steam flow rate was reduced, leading to a rising and then runaway bundle temperature (the FPT 0 test profile is shown in Fig. 4). The intention was to melt about 20% of the fuel bundle and produce a pool of molten material before shutting down the reactor. This was attained as can be seen in Fig. 5 which is a false colour X-ray radiograph of the fuel bundle produced at CEA Cadarache after testing. It is seen that virtually nothing of the fuel bundle remained in the middle section of the test assembly. This had melted and descended to form a central molten pool of corium at a height of 100–250 mm from the bottom of the fuel bundle, which had partially eaten into the protective ZrO_2 shroud. Below the corium pool the fuel rods were mostly intact. Likewise, at the top of the test assembly partial melting only had occurred and most of the fuel rods had survived.

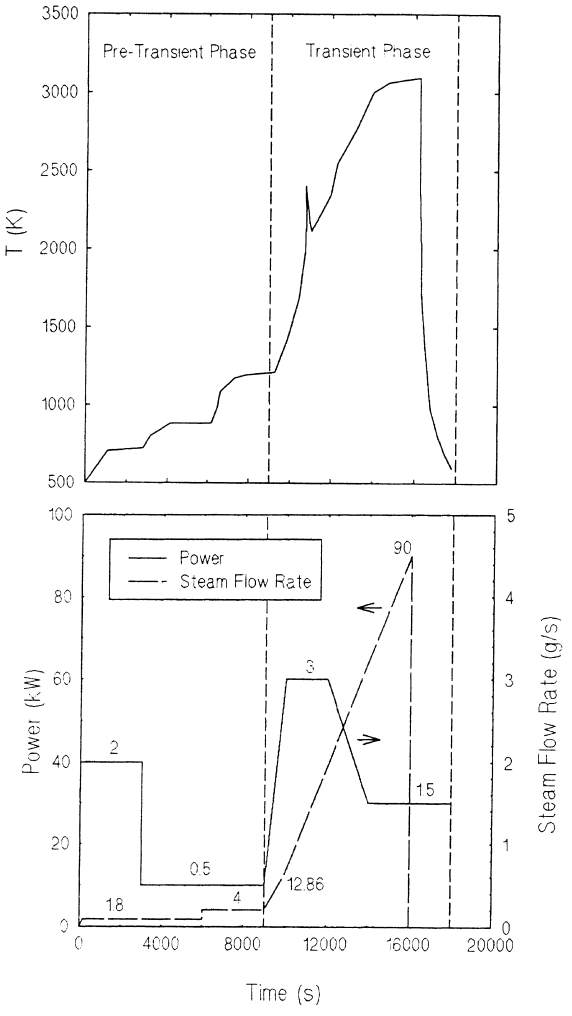

Fig. 4. The reactor power schedule, steam mass flow rate and temperature in the fuel bundle during the FPT 0 test (after Bottomley et al. [8]). The temperature is that at the position of thermocouple 10, i.e., at the centre of the fuel bundle at a height of 400 mm.

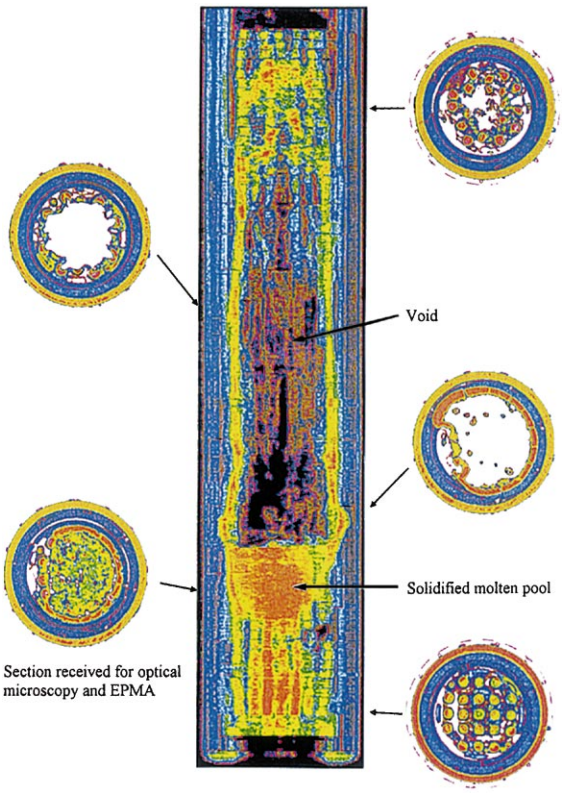

Fig. 5. False colour X-ray radiograph and computed tomography for five axial positions showing the condition of the FPT 0 fuel bundle at the end of the test. The material density increases in the order blue, green, yellow, red (after Bottomley et al.).

4. The samples

4.1. Melted fuel bundle

The section received at the Institute for Transuranium Elements was cut from the lower part of the solidified molten pool at a height of 149–172 mm from the bottom of the fuel bundle and identified as disc 3. The appearance of the upper surface that was examined is shown in Fig. 6. As seen, with the exception of a thin segment on the left, the molten pool extended

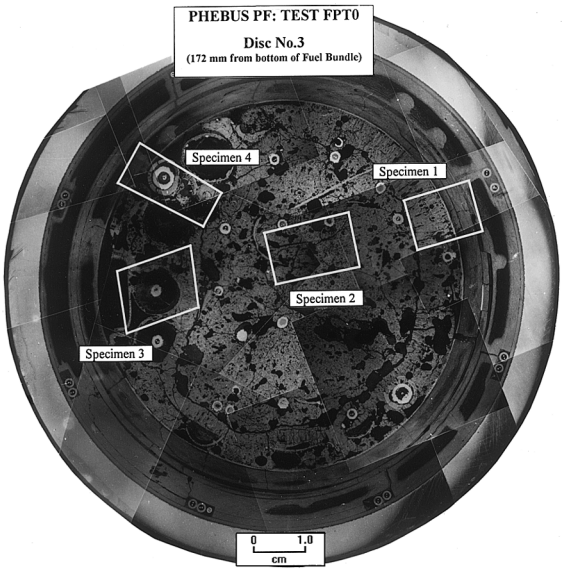

Fig. 6. Optical macrograph of disc 3 sent for post-test analysis at the Institute for Transuranium Elements (after Bottomley et al.). The locations of the specimens cut for optical microscopy and EPMA are shown.

over the whole cross-section. This exhibits an outer shell of columnar grains – typical for rapid cooling. Within the molten pool 17 thermocouples can be counted. Since prior to the experiment only three thermocouples were located at this level in the fuel bundle, it can safely be assumed that the other 14 had slumped down from higher axial positions in the test assembly. On the left, outside of the molten pool, a Zircaloy stiffener and two fuel rods containing thermocouples are visible. The stiffener and cladding of both fuel rods are severely oxidised and in some places have melted.

From the disc, four specimens were cut for optical microscopy and wavelength dispersive EPMA. The locations of these are marked in Fig. 6. Sample 1 from the edge of the molten pool included a region showing attack of the zirconia shroud. Sample 2 from the centre of the pool contained a thermocouple, Sample 3 comprised a stiffener and a degraded, but not melted, fuel rod and Sample 4 contained an ultrasonic thermometer.

4.2. Vertical line

Two samples cut from the vertical line were examined. One was a 2 cm high section from the 5 cm diameter tube at the base of the vertical line sited directly above the FPT 0 test bundle (see Fig. 2). The other was from the 3 cm diameter elbow union that connects the vertical line to the horizontal line leading to the simulated primary cooling circuit.

From the section removed from the bottom of the vertical line three specimens were cut for optical microscopy, SEM and energy dispersive microbeam analysis, γ-spectroscopy and ICP-MS. Specimens were taken from the lower end, upper end and central region of the elbow and submitted to a similar series of analyses.

5. Experimental

5.1. Specimen preparation

For optical microscopy and wavelength dispersive EPMA, specimens were vacuum impregnated with epoxy resin, cut from the disc using a SiC cutting wheel, and mounted in a special aluminium holder to facilitate handling by manipulators. After grinding on 400, 600 and 1200 grade SiC papers sprayed with water, the specimens were polished with 6 and 1 μm diamond paste using, as a lubricant, a 10% solution of ethylene glycol in ethanol. For final polishing a solution consisting of an alumina powder suspension, nitric acid, chromic acid and water was used. The atmosphere in the hot cells was partially deoxygenated air (N_2 – 5% O_2 max).

5.2. Optical microscopy

The specimens were examined on a Reichert Telatom 62 optical microscope installed in a hot cell. Certain specimens were additionally ion etched to improve optical contrast. The ion etching equipment was designed and constructed at the Institute. A low energy, low intensity beam of Ar^+ ions (acceleration voltage 8 kV; beam current 1 mA) about 10 mm in diameter was used. Etching was carried out in three, 15 min steps with two intermissions of roughly the same duration to allow the heat generated in the specimen to disperse. During etching the sample was inclined at an angle of 45° to the ion beam and slowly rotated at 20 rpm. Generally, areas of interest were examined at magnifications of 200 and 500×. At the latter magnification the limit of resolution is of the order of 0.5 μm.

5.3. Electron probe microanalysis

Wavelength dispersive EPMA was carried out using a Cameca MS 46 electron microprobe specially shielded with tungsten and lead to permit the analysis of irradiated nuclear fuel [3]. Analysis was performed on the optical microscopy specimens re-polished and coated with a 20 nm aluminium film to avoid charging effects. All elements were analysed at an electron acceleration potential of 15 kV and a beam current of 100 nA. (Except oxygen which was analysed at 10 kV.) *K*-values were calculated either from five or three peak and background determinations depending on the element

concentration level. The matrix correction was made using the PAP [4] option in the X-ray microanalysis program XMAS®, marketed by SAMx, France.

5.4. Scanning electron microscopy

Specimens cut from the samples from the vertical line were examined in a shielded JEOL 35C scanning electron microscope. This machine is equipped with a shielded secondary electron detector for the examination of radioactive materials [5]. The specimens were approximately 1×1 cm^2 in size and were mounted on a brass stub painted with a drop of epoxy glue on the upper surface. After hardening overnight, the specimens were coated with gold to avoid charging (Polaron equipment ES 200).

The electron microscope is equipped with a Tracor TN5500 energy dispersive analysis system which was used for X-ray microbeam analysis of the deposit in the vertical line.

5.5. Inductively coupled plasma mass spectrometry

ICP-MS was performed using an Elan 250 system marketed by Perkin–Elmer, which had been modified for installation in a glove box [6]. The rf generator power was 1.2 kW. The argon flow rates were 0.4 l m^{-1} for the nebuliser, 12 l m^{-1} for the plasma and 0.4 l m^{-1} for the torch. Measurements were made in the mass range 80–250 amu.

5.5.1. Melted fuel bundle

Powder samples from the solidified corium melt were micro-drilled out of the metallographic samples (0.5 mm diameter bit). One sample was taken from the columnar grains at the outer edge of the corium melt and a second from the centre of the melt. Approximately 3 mg of each sample was dissolved in 5 ml aqua regia at 180°C for 11 h; then the solution was diluted (25×) before an aliquot was taken for analysis. A second dilution (125×) was necessary for U determination. The calibration was carried out by spiking the solution with 1 ppm of indium and 1 ppm of thallium.

5.5.2. Deposits in the vertical line

Sections corresponding to a quarter ring were cut from the lower vertical line. In addition, a half ring was taken from the lower (vertical) end of the elbow and a whole ring from the upper (horizontal) end of the elbow. The centre of the elbow was also sampled by milling off the deposit from an approx. 25×12 mm^2 surface of the opened tube. The deposit taken from the lower vertical line weighed 340 mg whereas the total weight of the samples of deposit taken from the lower end, upper end and centre of the elbow was 1120 mg.

The deposits scraped off the sample of tubing from the bottom of the vertical line were digested successively in water, dilute nitric acid (0.1 M HNO_3) and concentrated nitric acid (7 M) for 3 days. Any residues remaining were dissolved in a mixture of 9HCl:1HNO_3:0.2HF at 190°C for 1 h. The solutions were then diluted (1300×) using distilled water to ensure that the combined concentrations of U and Pu in each aliquot was less than 500 ppm. Calibration was done again by spiking the solutions with 1 ppm of indium and thorium. The elbow deposits underwent a different procedure in which a second dissolution was made in dilute alkali (0.4 M NaOH) followed by one digestion directly with concentrated (7 M) nitric acid for 1 h at 185°C.

5.6. X-ray diffraction

X-ray diffraction was performed with a Siemens Kristalloflex DIFFRAC-11 diffractometer using monochromatic Cu $K\alpha_1$ radiation $\lambda=0.15406$ nm. The equipment was installed in a lead glass shielded glove box. The powder sample of corium weighing about 0.5 g was contained in a stainless steel phial provided with a thin beryllium window to allow the passage of X-rays. The diffraction pattern was recorded in the 2θ range 15–150° and the position of the diffraction lines corrected using an internal gold standard. The lattice parameter was calculated as the mean of all the lines observed using the DIFFRAC-11 dedicated computer programme.

5.7. Gamma spectrometry

The γ-spectrometer used a HPGe solid-state detector with an energy resolution of 1.8 keV at 660 keV (the energy of the γ-radiation from ^{137}Cs). The γ-spectrum was interpreted using the Intergamma® computer programme marketed by EURISYS, France. Energy calibration and the determination of the detector efficiency were made with a ^{152}Eu source.

Gamma spectrometry was carried out on the disc at the positions of rods 2, 11 and 15 and at the position of the central absorber rod (see Fig. 3). Rod 15 and the control rod had completely dissolved in the melt, whereas the rods 2 and 11 still existed but in a severely degraded state. At each rod position 36 γ-spectra were recorded using a 1.2×1.2 mm collimator and an acquisition time of 2000 s. The spectra were acquired from a 6×6 array of equi-distant points covering an area of 10×10 mm.

Gamma spectrometry on the lower vertical line was carried out on a specimen of near planar geometry 17×20 mm in size. The specimens cut from the lower and upper ends of the elbow measured 12×23 mm and 13×14 mm, respectively. The spectrum was collected from an area on the specimen measuring 10×10 mm

corresponding to the window in the lead shielding of the detector. The counting time was 3600 s.

6. Results for the fuel bundle

6.1. Matrix phase of the corium pool

EPMA of the central and outer regions of the corium pool revealed that the matrix phase was basically a solid solution of UO_2 and ZrO_2 containing traces of Fe (from the Inconel spacer grids and the stainless steel cladding of the control rod) and Y (from the stabilised zirconia thermal shroud). Its average chemical composition corresponded to $(U_{0.50}\ Zr_{0.47}\ Fe_{0.02}\ Y_{0.01})\ O_{2\pm x}$, where x is small.

The EPMA analysis results for the corium matrix are given in Table 1. It is seen that its composition was reasonably uniform, although in Specimen 2 the ceramic appeared to be markedly hypostoichiometric whereas in Specimen 3 it was almost stoichiometric (O/M ratio = 1.96 and 1.97).

The X-ray diffraction pattern obtained from the solidifed corium pool is shown in Fig. 7. It reveals that the matrix was a single phase with the fcc fluorite structure of UO_2 and a lattice parameter of 514.3 pm. Additional X-ray diffraction work performed by the Commissariat à L'Énergie Atomique, Saclay, on corium samples from different heights in the pool gave a similar fluorite type pattern with a lattice parameter of 526.2 pm which is intermediate between that for pure UO_2 ($a = 547.0$ pm) and that for pure cubic ZrO_2 ($a = 511.0$ pm, [7]). Significantly, peak doublets indicative of the presence of the higher uranium oxides (e.g., U_4O_9) were absent. Thus, little oxidation of the UO_2 fuel appears to have occurred.

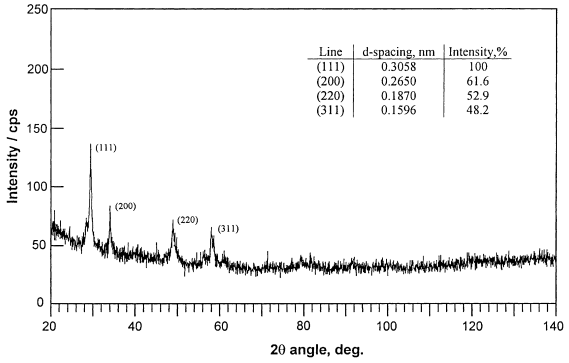

Fig. 7. X-ray diffraction pattern confirming the fcc fluorite crystal structure of the urania–zirconia solid solution forming the corium matrix.

The ICP-MS results for the corium are contained in Table 2. Only elements and isotopes with atomic mass greater than 80 were analysed. Consequently, the Fe measured by EPMA is not listed amongst the elements found. It is seen that the corium sample taken from the edge of the molten pool close to the zirconia thermal shroud was slightly richer in Zr. Interestingly this sample also contained significantly more Ag from the central control rod. This suggests that the grain boundary area was larger in the corium sample from the edge of the pool, since Ag is expected to accumulate at grain boundaries. Hafnium, W and Rh from the thermocouples were present in similar concentrations in both samples. Niobium, a constituent of Inconel from which the spacer grid clips were manufactured, was the only element present in appreciably higher concentrations in the sample from the centre of the melt. Molybdenum and Tc were the only fission products detected in the two corium samples.

Table 1
EPMA results for the corium matrix of the solidified molten pool[a] (after Bottomley et al. [8])

Location	Concentration (wt%)				
	Uranium	Zirconium	Yttrium	Iron	Oxygen
Specimen 1					
1	63.4 (2.3)	21.5 (1.3)	–[b]	0.8 (0.2)	–[b]
Specimen 2					
1	62.8 (1.4)	22.1 (0.4)	0.5 (0.1)	0.6 (0.1)	14.1 (0.5)
2	62.4 (1.7)	22.0 (1.2)	0.7 (0.2)	0.6 (0.1)	14.3 (0.4)
3	61.7 (1.2)	22.0 (0.7)	0.7 (0.1)	0.6 (0.1)	15.0 (0.2)
4	62.6 (1.0)	22.3 (0.2)	–[b]	0.5 (0.1)	–[b]
Specimen 3					
1	60.9 (0.7)	21.9 (0.7)	0.4 (0.3)	0.7 (0.1)	16.1 (0.5)
2[c]	62.5 (1.2)	21.1 (1.3)	0.0	0.5 (0.1)	15.8 (0.3)
3[c]	61.0 (1.2)	23.1 (1.4)	0.0	0.4 (0.1)	16.0 (0.4)

[a] Standard deviation is shown in parentheses.
[b] Not determined.
[c] Adjacent to melted Zircaloy cladding.

Table 2
ICP-MS results for the corium matrix of the molten pool[a]

Constituent	Concentration (wt%)	
	Centre[b]	Edge[c]
Uranium	58	61
Zirconium	22	27
Tin	0.06	0.06
Yttrium	0.54	0.72
Cerium	0.09	0.09
Silver	0.06	0.48
Hafnium	0.47	0.47
Tungsten	0.97	0.97
Rhenium	0.05	0.03
Niobium	0.24	0.08
Molybdenum	0.01	0.01
Technetium	0.02	0.01
Caesium	–[d]	–[d]

[a] Results for elements with masses below 80 are not included. For all values the relative error is of the order of 20%.
[b] In the region between Specimens 2 and 3 (see Fig. 6).
[c] At the location of Specimen 1 (see Fig. 6).
[d] Not detected.

The main fission product isotopes detected in the corium and degraded fuel rods by gamma spectroscopy were ^{137}Cs, ^{134}Cs, ^{106}Ru, ^{144}Ce and ^{95}Zr. The results for ^{137}Cs are shown in 3D display in Fig. 8. It is clearly seen that the concentration of this Cs isotope in the two degraded rods 2 and 11 was up to an order of magnitude higher than in the corium. This indicates that Cs, although highly volatile, was retained in small amounts in the degraded rods even though these had presumably seen temperatures of up to 2000°C in a steam atmosphere. The retained concentration is probably that part of the Cs dissolved in the UO_2 lattice.

6.2. Inclusions in the corium pool

Three types of inclusions were found in the corium pool; namely, spinels containing Fe, Cr and Ni, ReIr binary alloys of varying composition (in Specimen 2 an inclusion with 23% Re and another with 39 wt% Re were analysed) and W inclusions containing minor concentrations of Fe and Ni. In an earlier conference contribution the latter inclusions were mistakenly reported to be W oxide [8].

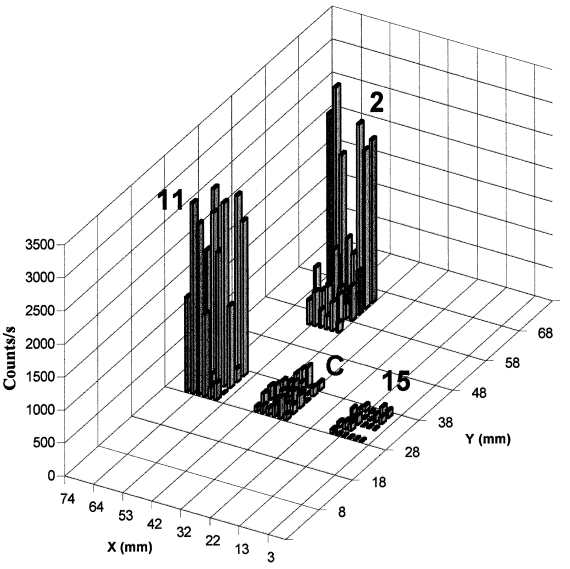

Fig. 8. Gamma scanning results for the concentration of ^{137}Cs in the degraded rods 2 and 11 and in the corium pool at the locations of rod 15 and the central control rod. *X* and *Y* are the specimen stage co-ordinates.

The composition of the spinel inclusions in the corium in Specimen 2 is given in Table 3. It can be seen that these were of two different compositions. Inclusion 1 contained high concentrations of all three elements whereas Inclusion 2 contained less then 1 wt% Cr.

6.3. The interaction between the corium melt and zirconia

The outer thermal shroud surrounding the fuel assembly and the thermal shrouds around the ultrasonic thermometers were made of zirconia.

Specimen 1 incorporated a section of the outer thermal shroud that had been attacked by the molten corium. The distribution in the interaction zone of the main constituents of the corium matrix (U, Zr, Fe and Y), as well as Ce, a constituent of the plasma-spray coating on the inner surface of the shroud, is shown in Fig. 9. It is seen that the width of the interaction zone, defined by the distance needed for the U concentration to fall from its level in the corium matrix (around

Table 3
Composition of the spinel inclusions in the corium in Specimen 2[a] (after Bottomley et al. [8])

Inclusion	Concentration (wt%)			
	Chromium	Iron	Nickel	Oxygen[b]
1	36.0 (0.8)	25.5 (0.7)	7.4 (0.1)	31.1
2	0.4 (0.1)	48.9 (0.6)	16.8 (0.1)	33.9

[a] Standard deviation is shown in parentheses.
[b] Determined by difference.

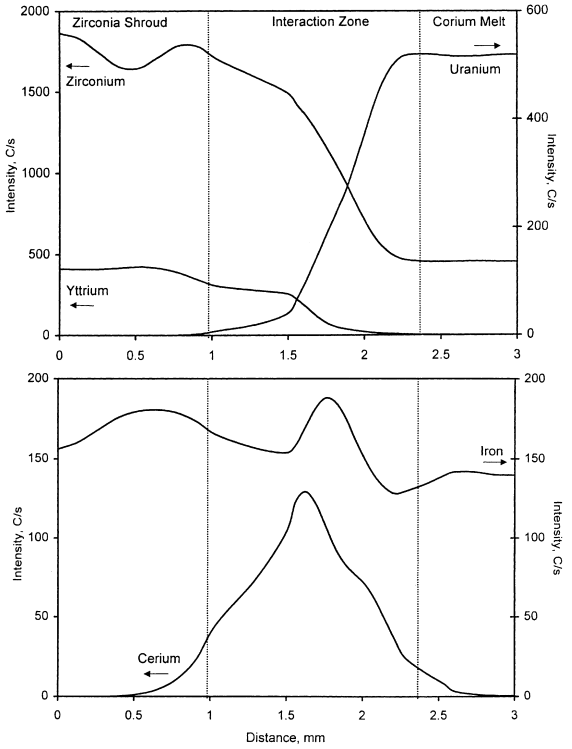

Fig. 9. X-ray line scans showing the distribution of U, Zr, Ce, Fe and Y across the interface between the thermal shroud and the corium melt in a region where chemical attack had occurred in Specimen 1. The Ce from the plasma-spray coating on the inner shroud surface has spread throughout the interaction zone and Fe from the corium melt has penetrated the shroud to a depth of 600 μm.

62 wt%) to zero, was about 1.25 mm. Cerium, although initially concentrated in a thin layer, 400 μm thick, had spread throughout the interaction zone and had even diffused about 600 μm into the corium and the zirconia. Moreover, it is also seen that Fe from the corium matrix had penetrated the zirconia shroud to a depth of at least 1 mm.

The zirconia shroud of the ultrasonic thermometer in Specimen 4 exhibited extensive intergranular cracking that was evidently related to the presence of extraneous material on the inner surface of the shroud. Clearly, this had entered the thermometer in the molten state through a breach in the shroud at a higher level in the assembly and had flowed down the inside of the tube. The material attached to inside of the shroud was a mixture of a urania–zirconia solid solution and a Fe–Cr–Ni spinel. Uranium and Fe from this mixture had penetrated the grains and grain boundaries equally to a depth of about 50 μm, but beyond this depth their intrusion was restricted to the grain boundaries. As seen from Fig. 10 even the grain boundaries at the centre of the shroud wall had been modified by the invasion of U, Cr, Fe and Ni.

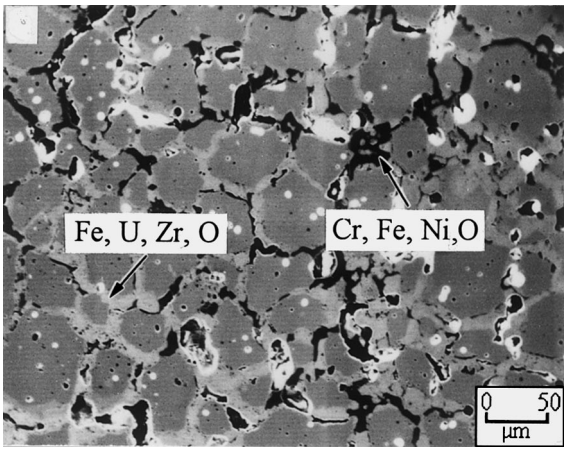

Fig. 10. Electron absorption micrograph of the zirconia thermal shroud of the ultrasonic thermometer in Specimen 4 showing intergranular attack at the centre of the shroud cross-section associated with the invasion of U, Cr, Fe and Ni from molten material (after Bottomley et al. [8]).

6.4. Interaction between the corium melt and thermocouple materials

Specimen 2 contained the remains of a thermocouple. During the test, molten corium containing Cr, Fe and Ni had penetrated the Re sheath of the thermocouple and reacted with the W and W–10Re wires and the HfO_2 insulator. Inside the sheath, the remains of a thermocouple wire could be discerned surrounded by a mass of material that had clearly been molten. It emerged that this material was the remains of the W–10Re wire. As seen from Fig. 11, this exhibited a fine eutectic-type microstructure composed of lamellae of a W rich phase and ReNi. At grain boundaries within this structure, phases rich in W, in U and in Hf and Zr, were identified, along with inclusions of Fe and occasionally Ni. The mass of material surrounding the wire also consisted of a U rich phase (probably UO_2), a phase rich in Zr and Hf (probably $(Zr,Hf)O_2$) and a W rich phase. These phases are assumed to be the same as the ones found on the grain boundaries in the degraded W–10Re thermocouple wire. The W contained in the material presumably came from the lost W wire.

It is to be noted that the Ir coating on the outer surface of thermocouple sheath had interacted with the underlying Re to a depth of about 80 μm forming an alloy containing 59 wt% Ir.

7. Results for core material deposited in the vertical line

A powder deposit covered the inside surface of the vertical line and elbow. In the lower part of the vertical

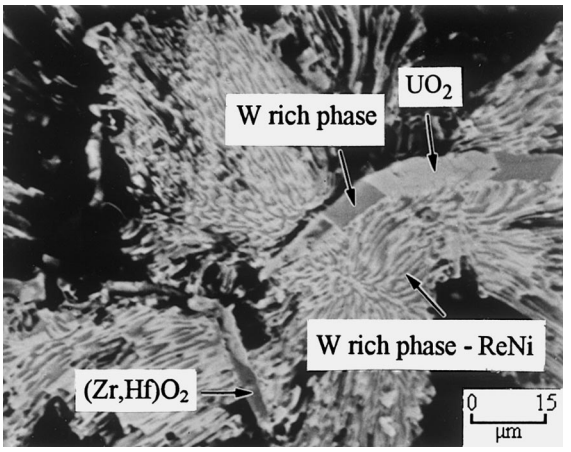

Fig. 11. Degraded W–10Re wire in the thermocouple in Specimen 2 (after Bottomley et al. [8]). The fine eutectic type structure is composed of lamella of a W rich phase and ReNi. The coarse phases at the grain boundaries are a W-rich phase and probably UO_2 and $(Zr,Hf)O_2$.

line the deposit was around 100 μm thick and had flaked in several places (Fig. 12). At locations where this had occurred the underlying oxidised steel surface was exposed. SEM at high magnification, revealed the individual powder granules which were about 10 μm in size to be agglomerates of sub-micron (⩽0.2 μm) aerosol particles. Embedded within the powder deposit were isolated spherical particles 10–20 μm in size. At the elbow the deposit was thinner and more adherent. It also contained noticeably fewer spherical particles.

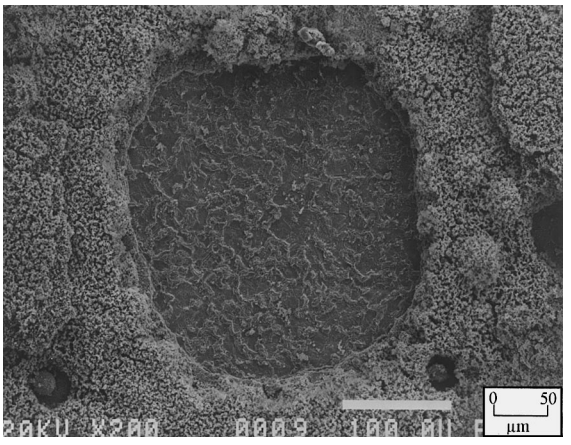

Fig. 12. SEM micrograph showing an area of deposit in the lower vertical line. In the centre of the micrograph, the deposit has spalled exposing the underlying steel surface, which is non-uniformly oxidised. The two spherical particles seen embedded in the deposit at the bottom of the micrograph are probably droplets of corium.

ICP-MS results for the deposits in the lower part of the vertical line and the elbow are given in Table 4. It is seen that Re from the thermocouple sheaths and In from the control rod, which were components of separate phases, were the main constituents of the deposits. Together these elements constituted 79 and 65 wt% of the deposits taken from the vertical line and elbow, respectively. Also contained in the deposits in concentrations greater than 2 wt% were U, Zr (elbow only), Sn, Ag and W. Tin amounted to almost 10 wt% of the deposit in the lower part of vertical line, whereas it constituted only 2.5 wt% of the deposit in the elbow. The ratio of the concentrations of U to Zr in the deposits was 5.1 and 4.0 which is considerably higher than the ratio of around 2.5 measured for the matrix of the corium pool.

It is pointed out that about 3% of the Re concentration was contained in the water eluent indicating that this percentage was probably oxide. Moreover, all but 0.3% of the Ag present was found in the 7 M HNO_3 and 9HCl:1HNO_3:0.2HF eluents implying that the Ag present in the deposit was almost entirely metallic.

The isotopes identified by γ-spectroscopy in a sample of deposit removed from the lower part of the vertical line and in samples taken from the lower end (vertical) and upper end (horizontal) of the elbow are listed together with their respective γ-activity in Table 5. It is clear from the Table that ^{137}Cs was mainly responsible for the γ-activity of the deposit on the inner surface of the vertical line. The concentration of this isotope was highest in the sample of deposit taken from the lower end of the elbow, which implies that turbulence in the bend may have disrupted the flow of released material into the horizontal line. Other isotopes detected in the deposit were ^{134}Cs (in the elbow only), ^{106}Ru (lower vertical line only), ^{110m}Ag and $^{95}Zr/Nb$. All these

Table 4
ICP-MS results for the deposit in the lower vertical line and elbow[a]

Constituent	Concentration (wt%)	
	Vertical line	Elbow
Uranium	2.2	17
Zirconium	0.43	4.2
Tin	9.6	2.5
Silver	3.7	2.9
Tungsten	3.1	4.1
Rhenium	62	54
Indium	15	10
Cerium	<0.01	0.13
Molybdenum	0.47	0.54
Technetium	<0.01	–[b]
Palladium	–[b]	0.18
Caesium	–[b]	–[b]

[a] Results for elements with masses below 80 are not included. For all values the relative error is of the order of 20%.
[b] Not detected.

Table 5
Gamma-spectroscopy results for the lower vertical line and elbow[a]

Isotope	Gamma activity (MBq)		
	Lower vertical line	Elbow	
		Lower end[b]	Upper end[c]
^{60}Co	0.123	0.018	0.023
^{95}Zr/Nb	0.084	0.132	0.031
^{99}Mo	–[d]	0.008	–[d]
^{110m}Ag	1.078	–[d]	0.444
^{125}Sb	0.700	–[d]	0.131
^{106}Ru	0.097	–[d]	–[d]
^{134}Cs	–[d]	0.592	0.427
^{137}Cs	8.460	10.150	1.228
Total	10.458	10.900	2.284

[a] The measurements were made in January 1996 (lower vertical line) and April 1996 (elbow samples). The FPT 0 test was carried out in December 1993.
[b] Vertical.
[c] Horizontal.
[d] Not detected.

isotopes except ^{110m}Ag are fission products. The isotope ^{110m}Ag is a product of the irradiation of the Ag in the control rod alloy. Curiously, this isotope was apparently not detected in the sample of deposit from the lower end of the elbow, although the γ-activity resulting from its presence in the other two samples was significant.

Fig. 13 shows a cluster of spherical particles in the deposit in the lower part of the elbow. Deposited on the surface of these particles are cuboidal crystallites. Energy dispersive X-ray microanalysis revealed U and Zr to be the main metallic elements in the particles. The crystallites covering the surface of the particles were found to be mainly In and Re. The energy dispersive spectrum revealed the presence of In:Re:Ag:W in the mass ratio 12:4:1:1.

A vertical section through the deposit in the lower part of the vertical line is shown in Fig. 14. The deposit had broken into two parts during specimen preparation. Energy dispersive X-ray microanalysis across the section revealed that the deposit consisted of several strata of different composition. The first layer at the steel surface was about 2 μm thick and was rich in Ni and Sn. Above this layer, the deposit was a mixture of In, Ag and Re. At the deepest level the deposit was In oxide containing roughly 40 wt% Ag, whereas the outer 50 μm of the deposit was essentially pure Re. The change in composition occurred over several tens of microns. Noticeable amounts of Re first appeared in the deposit at 10 μm from the steel surface. Silver was not detected at distances greater than 35 μm from the steel surface and both Ag and In were absent from the deposit at 80 μm from the steel surface.

Nickel at concentrations estimated to be between 1 and 5 wt% was found throughout the deposit. In the lower regions of the deposit, up to 1 wt% Cr and 2 wt% Fe were also detected. It is assumed that these steel constituents had diffused into the deposit from the underlying Inconel wall of the vertical line.

It is seen from Fig. 14 that although the bulk of the deposit was porous, the first material laid down (Sn followed by In and Ag) formed dense compact layers. In contrast, the layer of Re and In beneath the thick deposit of Re forming the outermost layer contained numerous large cavities. The increase in porosity in the outer regions of the deposit is attributed to an increase

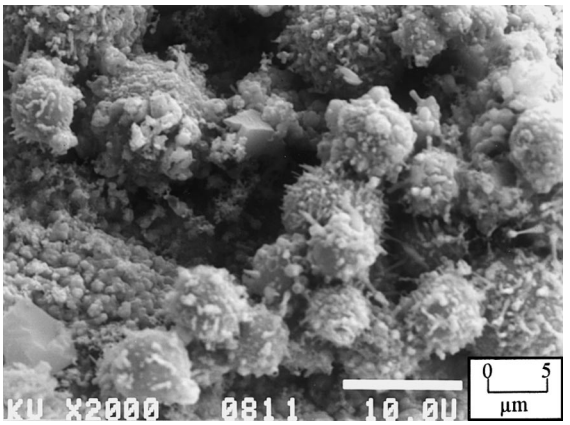

Fig. 13. SEM micrograph of a cluster of corium droplets in the deposit at the lower end of the elbow. The surfaces of the droplets are coated with crystallites rich in In and Re.

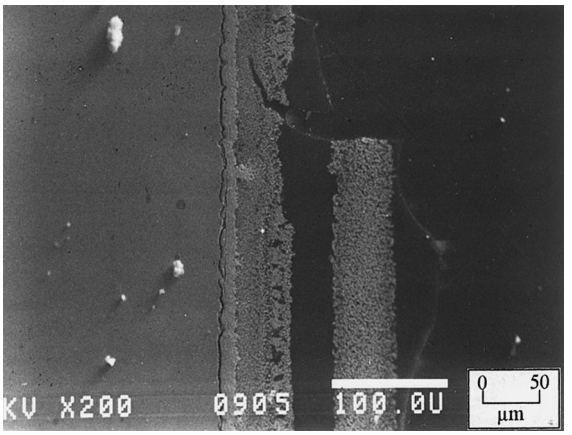

Fig. 14. SEM micrograph of a vertical section through the deposit in the lower vertical line. The deposit exhibits four major strata. The innermost one is composed mainly of In and Ag. This is followed by two layers of markedly different density composed mainly of In and Re. The outermost layer, which has spalled during specimen preparation, is essentially pure Re.

in the agglomeration of the aerosol particles as the test progressed. Either an increase in the time in suspension or an increase in the rate of aerosol formation was responsible for this. Measurement of the aerosol density downstream of the vertical line using photo-absorption clearly showed that aerosol formation increased in the final stages of the test and again on shutdown.

8. Discussion

8.1. Corium and its interaction with the components of the test bundle

EPMA on Specimens 1, 2 and 3 revealed that the corium matrix of the solidified molten pool was uniform in composition. This would indicate that the phase had been fully molten with strong convection currents leading to complete mixing. The corium matrix was found to contain approximately 62 wt% U, 22 wt% Zr, 0.6 wt% Fe and 0.6 wt% Y. Using the laser flash technique the temperature at which corium starts to melt was determined to be 2230°C (C. Ronchi and M. Sheindline, Institute for Transuranium Elements, personal communication). This is about 250°C lower than the melting point minimum in the UO_2–ZrO_2 phase diagram of Romberger et al. [9] which is the one considered most reliable [10]. Trace elements in the corium, particularly Fe, could be responsible for the lower value. However, Uetsuka et al. [11] noted very little influence of iron oxide content on the melting point of corium in material simulating debris from the Three Mile Island reactor accident. This has been confirmed by thermodynamic calculations which have shown that 2–3 wt% Fe_2O_3 lowers the UO_2–ZrO_2 melting point by only 50 K and hence cannot explain the discrepancy between the Ronchi data and the literature.

The highest temperature reached by the corium melt in FPT 0 was probably in excess of 2900°C. This is deduced from the fact that above the molten pool the corium had consumed almost three-quarters of the 11.5 mm wall thickness of the ZrO_2 thermal shroud with a melting point of about 2700°C (see Fig. 5). In the molten pool, however, the corium appears to have been at a temperature not much above its melting point. This is apparent from the fact that dissolution of the thermal shroud was not detected in disc 3, although some interdiffusion of the zirconia and corium constituents had taken place. Further, the solidified melt exhibited a cast structure consisting of an outer shell of columnar grains and a core of equiaxed grains. Such structures generally result when a melt is cooled from a temperature that is slightly above the freezing point.

Since the corium matrix was uniform in composition it follows that cooling had been sufficiently rapid to retain the high-temperature cubic $(U,Zr)O_2$ phase and suppress the formation of the tetragonal and monoclinic phases. This was confirmed by X-ray diffraction. However, the stability of the high-temperature cubic phase may have been partly enhanced by the presence of Y_2O_3 in the melt. It is pointed out that samples taken from the melted core of the TMI–2 reactor contained both the intermediate-temperature Zr rich tetragonal and the high-temperature U rich cubic phases [12]. Thus, in the TMI accident the molten core had cooled more slowly. From the spacing of the tetragonal and cubic phases it was estimated that the molten core had solidified over a period of 7 h. In contrast, the corium formed in FPT 0 had solidified in a matter of minutes.

EPMA of the Zr rich tetragonal and U rich cubic phases in corium samples from the TMI-2 reactor revealed that the former phase contained 12.7 wt% U and the latter 1.6 wt% Zr [13]. Area analysis of the UO_2–ZrO_2 corium matrix in a region where spinel inclusions were absent indicated that its average composition was 61.9 wt% U, 20.8 wt% Zr and 17.3 wt% O. Thus, the overall composition of the two phase matrix of the TMI-2 corium is very similar to that of the UO_2–ZrO_2 solid solution which formed the matrix of the corium in FPT 0. Consequently, it appears that the matrix composition of the melted core of a thermal reactor always tends to be close to an equi-molar solution of UO_2 and ZrO_2. This could be because this composition exhibits the minimum melting temperature in the UO_2–ZrO_2 system [10] or simply because much more Zircaloy than UO_2 is melted. The latter is confirmed by the fact that in both TMI-2 and FPT 0, the Zr concentration of the corium matrix (20.8 and 22 wt%, respectively) was substantially higher than the typical PWR inventory of roughly 16 wt% [14].

The metallic and oxide inclusions in the solidified corium pool had clearly formed from material that had separated when the melt cooled. Since one of the ReIr inclusions analysed was of similar composition to the ReIr alloy at the surface of the thermocouple sheath in Specimen 2, it follows that the origin of these inclusions was the dissolution of this alloy which has a melting point of (2800 ± 25)°C [15]. The concentrations of Fe and Ni in the W inclusions were not analysed. Sykes reports [16], however, that up to 0.8 wt% Fe is soluble in solid W and according to Kozma and Labár [17] the solubility of Ni in solid W decreases from 0.2 wt% at 1927°C to 0.02 wt% at about 1200°C. The melting point of W is 3410°C which is at least 300°C higher than the highest temperature reached by the corium melt. Nevertheless, the finding of W inclusions is consistent with the knowledge that this element has a solubility in UO_2 of about 5 wt% at the latter's melting point (C. Ronchi, personal communication). Consideration of the high melting points of the ReIr inclusions and of W leads to the conclusion that the spinel inclusions with a melting

point close to 1600°C (m.p. of Fe_3O_4 is 1594°C [18]) were the last to solidify.

The zirconia components in disc 3 exhibited not only attack by the molten corium, but also interaction with Cr, Fe and Ni. In Specimen 1, Fe from the corium had diffused into the inner zirconia thermal shroud in advance of the dissolution front to a depth of at least 1 mm (see Fig. 9). Further, in Specimen 4, molten corium containing high concentrations of Fe, Cr and Ni had penetrated along the grain boundaries of the thermal sheath of the ultrasonic thermometer and on cooling had formed a separate (Cr, Fe, Ni) spinel phase leaving on each side of the grain boundaries a strip enriched in U and Fe (see Fig. 10). The tendency for Cr, Fe and Ni (presumably as liquid oxides) to penetrate zirconia has led to the decision to use thoria for the thermal shrouds in future Phebus tests.

The thermocouple wires and spacer pellets were also susceptible to attack by the corium melt and molten steel components. In the case of the thermocouple in Specimen 2, Ni had alloyed with the Re in the W–10Re wire which had transformed from a solid solution (m.p. approx. 2800°C) to a fine two-phase mixture composed of ReNi and a W rich phase (see Fig. 11) via a peritectic reaction at 1620°C. At the peritectic point 40.1 wt% Re is soluble in Ni [19]. Further, Zr from the corium had combined with HfO_2 from the spacer pellet leaving a UO_2-rich phase on the grain boundaries.

8.2. The material deposited in the vertical line

Rhenium was the main constituent of the deposits on the inner surface of the vertical line and the elbow. It was almost certainly transported in the form of one of its higher, more volatile oxides, since Re metal is refractory (m.p. of Re is 3180°C [20]). The samples of deposit examined showed clear stratification, indicating that the composition of the atmosphere in the vertical line had changed several times during the test as the different components of the fuel bundle melted and volatilised. The Sn that coated the steel surface of the vertical line almost certainly came from the Zircaloy fuel cladding. Tin is barely soluble in ZrO_2 and αZr(O) [21,22] and consequently is rejected by the Zircaloy when the cladding oxidises. Contrary to what has been reported (e.g., Ref. [23]), the finding that Sn was deposited in advance of Ag and In would suggest that significant oxidation of Zircaloy occurred at the beginning of the test before the central control rod ruptured. In the deeper levels of the deposit, the higher concentration of In compared with Ag is consistent with its higher volatility. Moreover, the presence of small amounts of Re in the lower layers reveals that oxidation of the thermocouple sheaths also began early in the test. Very little or no Ag and In was detected in the outer region of the deposit which was essentially pure Re. From this it is deduced that the control rod, except at the lower level below the corium pool, was consumed well before the test was completed.

The spherical particles containing U and Zr are solidified droplets of molten corium. However, the ICP-MS analysis results indicate that the particles have a U/Zr ratio roughly twice that of the solidified corium matrix. This suggests that the particles were released during the formation of the molten pool, before it had reached its final composition. The heavy corium particles found in the elbow at the top of the vertical line had travelled more than 3 m in the steam-flow. The In-rich crystals found on the surface of the corium particles in the lower part of the elbow are assumed to have grown by condensation of In vapour (either as the oxide or the metal) on the solidified corium particles. Considering the high boiling point of In (≈2000°C), it seems reasonable to assume that if the crystals were deposited as the metal, they condensed before the corium particles had reached the vertical line.

9. Conclusions

The corium matrix of the solidified molten pool was a single phase of composition $(U_{0.50}Zr_{0.47}Fe_{0.02}Y_{0.01})O_{2\pm x}$, where x is small, with first melting at about 2250°C. The presence of minor concentrations of Fe and Y cannot explain the low melting of the solid solution. The corium melt had reached a temperature of at least 2900°C, but at the axial location of disc 3 examined in the present study it had cooled from a lower temperature. The rate of cooling had been sufficient to stabilise the high temperature cubic phase and to inhibit separation of the Zr rich tetragonal and U rich monoclinic $(U,Zr)O_2$ phases. The corium matrix contained an increased level of Zr compared with the overall FPT 0 core inventory. Since the TMI-2 corium was also enriched in Zr, this may represent a general tendency in corium pool formation.

Inclusions in the corium contained constituents originating from the fuel rod springs and structural materials (stainless steel cladding of the control rod, Inconel grid spacers, etc.) and from thermocouple components. The inclusions detected in disc 3 by EPMA were of three types; namely, ReIr binary alloys of varying composition, W with minor concentrations of Fe and Ni and spinels based on Fe, Cr and Ni, also of varying composition. These had formed early in the cooling process when the corium melt solidified. Silver from the control rod had limited solubility in the corium melt and during solidification it segregated to the grain boundaries. Liquid corium acted aggressively towards the zirconia thermal shrouds and resulted in the intergranular attack of these components. This attack was enhanced by the presence of Fe, Ni and Cr in the melt.

Degraded fuel rods that have been exposed to temperatures up to 2000°C in steam can retain some Cs. The

Cs concentration in the two degraded rods 2 and 11 in disc 3, was an order of magnitude higher than in the solidified corium pool at the position of rod 15. This suggests that Cs is completely released from the fuel only when melting occurs.

Rhenium from the thermocouple sheaths and Ag together with In from the central control rod were the main constituents of the deposit on the inside surface of the vertical line and elbow. The individual powder granules, which were about 10 μm in size, were agglomerates of sub-micron ($\leqslant$2 μm) aerosol particles. A thin layer of Sn was present on the steel surface of the vertical line. This was ejected from the Zircaloy fuel cladding during its oxidation at the beginning of the test. Indium was transported as a vapour in the vertical line, whereas Re (as oxide) and Ag (probably as metal) were present as aerosols. Solidified droplets of molten corium were embedded in the deposit. Indium-rich crystals were often attached to the surface of these droplets. These crystals resulted from the condensation of In vapour (either as the oxide or the metal). Traces of ^{137}Cs were mainly responsible for the γ-activity of the deposit.

References

[1] P. von der Hardt, A. Tattegrain, J. Nucl. Mater. 188 (1992) 115.
[2] Ph. Delchambre, P. von der Hardt, Phebus-FP test facility, in: W. Krischer, M.C. Rubinstein (Eds.), The Phebus Fission Product Project, Elsevier, Amsterdam, 1992, p. 159.
[3] C.T. Walker, in: Proceedings of the Second Regional EMAS Workshop on Modern Developments and Applications in Microbeam Analysis, Kossuth Lajos University, Debrecen, Hungary, 1996, p. 102.
[4] J.L. Pouchou, F. Pichoir, Un nouveau modèle de calcul pour la microanalyse par spectrometrie de Rayons X partiel: Application à l'analyse d'Echantillons homogènes, La Recherche Aérospatiale 5 (1984) 167.
[5] M. Coquerelle, P. Knappik, J.-C. Perrier, J. Phys. (Paris) 45 (C2) (1984) 84.
[6] J.I. Garcia Alonso, F. Sena, P. Arbore, M. Betti, L. Koch, J. Anal. At. Spectrom. 10 (1995) 381.
[7] K.H. Hellwege, A.M. Hellwege (Eds.), Landolt-Börnstein: Zahlenwerte and Funktionen aus Naturwissenschaften and Technik, NS, III/7/b1, Springer, Berlin, 1975, p. 324.
[8] P.D.W. Bottomley, F. Montigny, A.D. Stalios, C.T. Walker, Mikrochim. Acta (Suppl 15) (1998) 191.
[9] K.A. Romberger, C.F. Baes, H.H. Stone, J. Inorg. Nucl. Chem. 29 (1967) 1619.
[10] H. Kleykamp, R. Pejsa, Chemical and X-ray Diffraction Analysis on Selected Samples from the TMI-2 Reactor Core, Kernforschungszentrum Karlsruhe Report KfK 4872, 1991.
[11] M. Uetsuka, Thermal Property Measurements of TMI-2 Simdebris, SARJ-94, 31 October–1 November 1994, Tokyo, Japan.
[12] A. Braun, G.J. McIntyre, C. Gräslund, Nucl. Technol. 87 (1989) 137.
[13] P.D.W. Bottomley, M. Coquerelle, Nucl. Technol. 87 (1989) 120.
[14] In-Vessel Core degradation in LWR Severe Accidents – A State of the Art Report to CSNI, Report OECD/NEA/CSNI/R(91), 1991.
[15] T.B. Massalski, H. Okamoto, P.R. Subramanian, L. Kacpzak (Eds.), Binary Alloy Phase Diagrams, vol. 3, ASTM International, Materials Park, OH, 1990, p. 2346.
[16] W.P. Sykes, Metal Handbook, American Society of Metals, Cleveland, OH, 1948, p. 1220.
[17] L. Kozma, J. Labár, High Temp.-High Press. 13 (1981) 521.
[18] D.R. Lide, H.P.R. Frederukse (Eds.), Handbook of Chemistry and Physics 1993–1994, 74th Ed., CRC, Boca Raton, 1993, p. 4–91.
[19] T.B. Massalski, H. Okamoto, P.R. Subramanian, L. Kacpzak (Eds.), Binary Alloy Phase Diagrams, vol. 3, ASTM International, Materials Park, OH, 1990, p. 2847.
[20] D.R. Lide, H.P.R. Frederukse (Eds.), Handbook of Chemistry and Physics 1993–1994, 74th Ed., CRC, Boca Raton, 1993, p. 4–66.
[21] S.R. Mulpuru, R.R. Rondeau, E.N. Luidquist, Trans. Am. Nucl. Soc. 69 (1993) 313.
[22] C.A. Alexander, J.S. Ogden, J. Nucl. Mater. 175 (1990) 197.
[23] J. Lewi, M. Schwarz, P. von der Hardt, Atomwirtschaft 43 (1998) 92.